Defect identification in semiconductors by Brewster angle spectroscopy

H. J. Lewerenz and N. Dietz
Hahn-Meitner-Institut, Bereich Photochemische Energieumwandlung, Postfach 39 01 28, Glienicker Strasse 100, D-1000 Berlin 39, Germany

(Received 3 August 1992; accepted for publication 15 January 1993)

The sensitivity of the pseudo Brewster angle φ_B and the reflectivity for p-polarized light at this angle $R_p|\varphi_B$ to small changes in absorption is used for the identification of deep and shallow defects in semiconductors. Brewster angle spectroscopy (BAS) was performed on undoped and n-type GaAs as well as on undoped and p-type InP. Comparison with literature values shows that BAS can be used to identify deep defects at room temperature without electrical contacting. The changes in the spectra of undoped and doped GaAs and InP can be explained by involving the respective donor and acceptor levels in the transition processes. For $CuInS_2$ the defects are analyzed by measuring R_p close to φ_B as a function of photon energy. The findings can be explained on the basis of existing photoluminescence data, postulating two additional deep levels at $h\nu=E_v+0.350$ eV and $h\nu=E_v+0.625$ eV. The comparison of model spectra for shallow defects with φ_B spectra of $CuInS_2$ grown with sulphur excess leads to identification of a level at $E_v+0.015$ eV in accordance with luminescence data on the energetic position of sulphur interstitials. The applicability of BAS is shown, taking into account the experimental limitation through depolarization and angle divergence.

I. INTRODUCTION

Semiconductor materials development and optimization depends to a large extent on the possibility to correlate processing parameters with defect concentration and energy.[1-6] Particularly important is the energetic identification of defect levels within semiconductor band gaps which largely define bulk recombinative behavior in devices. Various experimental methods have been applied for the analysis of defect centers. Techniques such as photoluminescence (PL),[7,8] cathodoluminescence,[9] photocapacitance spectroscopy (PCS),[8,10-12] or deep level transient spectroscopy (DLTS)[5,13-15] require electrical contacting and/or sample cooling. Contactless measurements which are mainly optical methods as for instance electroreflectance (ER),[16,17] photoreflectance (PR),[16] photothermal deflection spectroscopy (PDS),[18] and standard reflection–absorption measurements[19,20] are limited in sensitivity or applicability.

We present here an optical method with enhanced sensitivity which is achieved by a reflectivity extinction condition. If in an idealistic view, a semiconductor at photon energies below its band gap energy is considered transparent (neglecting band tails), a well defined Brewster angle should exist for which the reflected electric field component polarized parallel to the plane of incidence r_p vanishes. The existence of an absorbing center within this energy regime would relax the Brewster angle law,[21-23] resulting in a shift of the angle at which $dR_p/dE_{\mathrm{Ph}}=0$ (R_p: reflectivity for p-polarized light) and in an offset, i.e., $R_p>=0$.[22,23] In real semiconductors and metals, a pseudo Brewster angle[24] is observed and the band tails result in a complex dielectric function ϵ within the energy gap. It is therefore of interest to investigate the possibility of identifying an absorption structure due to defect levels superimposed on band tails by using Brewster angle geometry in which the sample can be viewed as a polarizer element suppressing s-light components.

II. EXPERIMENT

The experimental arrangement is schematically shown in Fig. 1. As light source a tungsten iodine lamp with a Kratos monochromator was used. The parallel monochromatic light beam is split into a reference and a signal channel, detected at D_1 and D_2, respectively. The signal beam is polarized parallel to the plane of incidence, using a Glan–Thompson polarizer P. The extinction ratio of P is smaller than 10^{-6} in the wavelength range from 215 nm to 2.3 μm. The polarized light is focused onto the sample held at an angle φ close to the Brewster angle φ_B. The reflected intensity is detected by a cooled Si (0.4–1 μm) or Ge detector (0.8–1.7 μm). The detected signals (D_1 and D_2) are processed using preamplifiers (Keithley 428) and a lock-in amplifier (EG&G 5210). For analysis of the reflected intensity and the Brewster angle position, the signal at D_2 is measured as a function of the angle φ. The measured angular range near φ_B is chosen automatically, by the following procedure: first, the Brewster angle is centered in the interval; second, the interval range is chosen such that the data from the lock-in amplifier output lie in the range 0.1–10 V. Depending on the absorption of the material the measured angular ranges lie between 1° for weak absorption and about 5° for strong absorption. The Brewster angle and the intensity at that angle are determined by a parabolic least square fit of the measured angular range. Therefore the chosen angular range is also defined by the parabolic approximation condition which is used to determine the Brewster angle. The applicability of this approximation for reflectivity data near the Brewster angle has been shown by Miller *et al.*[25] The associated reflectivity $R_p|\varphi_B$ was determined by comparison of the reflected intensity at φ_B with the signal at the detector D_1. The accuracy of the

 0021-8979/93/104975-13$06.00 © 1993 American Institute of Physics

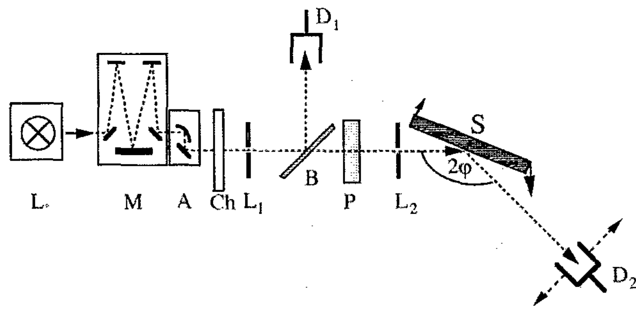

FIG. 1. Schematical drawing of the experimental setup; L: lamp; M: monochromator; A: mirror focus unit; L_1, L_2: slits; Ch: Chopper; B: beamsplitter; P: polarizer; D_1, D_2: detectors; S: sample.

method depends critically on the angular resolution of the goniometer table on which the sample is mounted. The mechanical specification yields a resolution better than 2×10^{-3} deg for the relative angular position. The influence of angle divergence and depolarization are discussed in Appendix B. For the determination of the absolute angular position an error of smaller than 0.1° has to be assumed. The absolute position, however, is only important for the analytical calculation of the optical constants of the material. An assumed error of 0.1° in the absolute position yields a relative error of 0.1% in the determination of the optical constants ϵ_1 and ϵ_2. The interrelation between the complex dielectric function $\hat{\epsilon}$ with the measured Brewster angle and reflectivity at this angle is given in Appendix A. The step motor limitation results in a resolution of 4×10^{-3} deg. To determine the first and second derivative of the measured Brewster angle spectra, an algorithm based on a compensation method (quadratic least squares fit) was used.[26] The algorithm also provides the smoothing of the spectra in such way that every data point x_i of a spectrum was approximated by a parabolic function in the interval $[x_{i-n/2},x_i,x_{i+n/2}]$ (n: variable index). The formation of the first and second derivative was also carried out by a Snyder algorithm[27] and compared with the parabolic compensation method. Both methods are discribed in Appendix C.

For testing the sensitivity of the method as well as the accuracy of the optical elements, the semiconductors

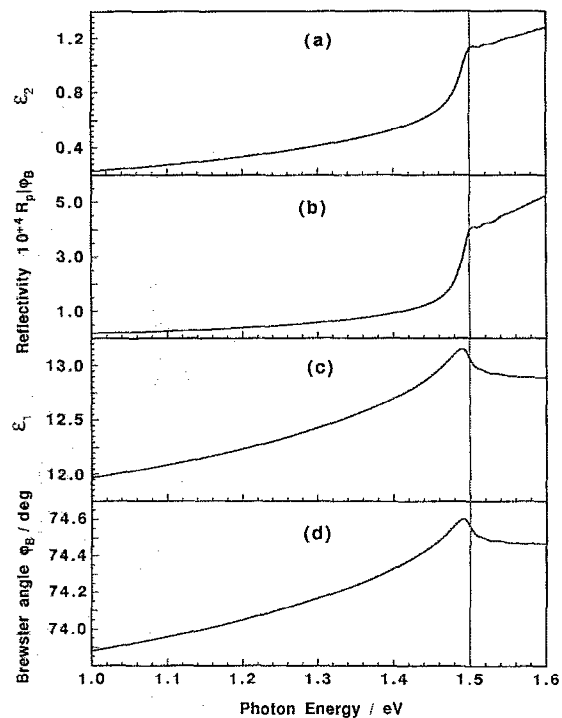

FIG. 2. Calculated optical properties for a simulated dielectric function ϵ generated by Lorentz oscillators. The assumed data for the Lorentz oscillator are chosen such that the optical behavior is similar to the properties of CdTe.

GaAs and InP are investigated. GaAs and InP were obtained from MCP-Wafer Technology Ltd. (England) and grown using the high-pressure Bridgman method. Table I summarizes the electronic properties of the wafers investigated. All wafers were polished on both sides with the front surface etched. No further surface cleaning was done. After mounting in the goniometer sample holder, a nitrogen stream was introduced to prevent oxidation during the measurement. For the simulation of the optical properties of defects, data of CdTe were used because CdTe has a direct band gap of 1.5 eV, very similar to the ternary chalcopyrite $CuInS_2$ which is an important solar cell material.

The investigated $CuInS_2$ crystals were grown with the gradient freeze technique[28] by using argon overpressure

TABLE I. Electronic properties of investigated samples.

Compound	Type	Orientation	Dopant	$\|N_A-N_D\|$ [cm^{-3}]	R [Ω cm]	μ [cm^2 V^{-1} s^{-1}]
GaAs	n	(100)	nil	3.6×10^{15}	⋯	5640
	n	(100)	Sn	2×10^{17}	⋯	3000
InP	n	(100)	nil	5×10^{15}	0.27	5000
	n	(100)	Sn	1×10^{18}	⋯	⋯
	p	(100)	Zn	1×10^{18}	⋯	⋯
	p	(100)	Cd	1.2×10^{18}	0.07	80.2
$CuInS_2$	p	(112)	S excess	⋯	2.5×10^{-3}	7
	n	(112)	In and S excess	⋯	⋯	a
	i	(112)	nil	⋯	⋯	a

[a]Resistance of the material too high.

TABLE II. Assumed data for the Lorentz oscillator to build up the spectra in Fig. 2. The given oscillator strengths are relative. The sum of all oscillator strength are normalized to 1 in the computer program.

k	E_k	G_k	S_k	k	E_k	G_k	S_k
1	1.50	0.03	0.10	22	1.92	0.32	0.17
2	1.52	0.03	0.05	23	1.94	0.33	0.18
3	1.54	0.04	0.06	24	1.96	0.34	0.18
4	1.56	0.06	0.08	25	1.98	0.35	0.20
5	1.58	0.09	0.10	26	2.00	0.36	0.25
6	1.60	0.10	0.11	27	2.10	0.37	0.30
7	1.62	0.12	0.12	28	2.20	0.38	0.35
8	1.64	0.14	0.12	29	2.30	0.39	0.40
9	1.66	0.16	0.13	30	2.40	0.40	50.45
10	1.68	0.18	0.13	31	2.50	0.40	1.00
11	1.70	0.20	0.13	32	2.60	0.40	2.00
12	1.72	0.22	0.14	33	2.70	0.40	3.00
13	1.74	0.23	0.14	34	2.80	0.50	4.00
14	1.76	0.24	0.15	35	2.90	0.50	5.00
15	1.78	0.25	0.15	36	3.00	0.50	5.00
16	1.80	0.26	0.15	37	3.10	0.50	5.00
17	1.82	0.27	0.15	38	3.20	0.50	5.00
18	1.84	0.28	0.16	39	3.40	0.80	20.00
19	1.86	0.29	0.16	40	3.60	0.80	20.00
20	1.88	0.20	0.16	41	3.80	0.80	20.00
21	1.90	0.31	0.17	42	4.00	0.80	20.00

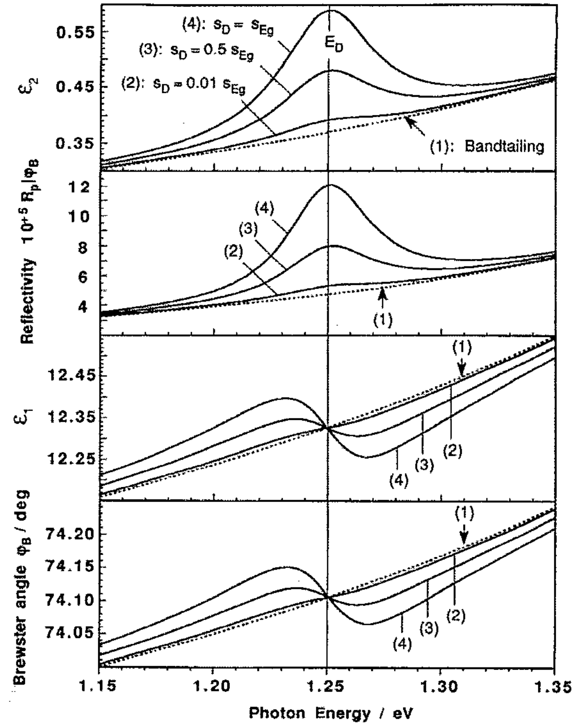

FIG. 3. Influence of a small defect oscillator with various oscillator strengths and an assumed damping constant of 50 meV within the band gap.

(25 bar at the melting point) during the growth from its melt.[29] The cleaved samples were characterized by Debye–Scherrer diffraction and Laue diffraction patterns and show [112] orientation.[30]

III. MODEL CONSIDERATIONS

This section provides the basic mathematical expressions which describe the interrelation between defect absorptivity within a semiconductor band gap and the complex dielectric function $\hat{\epsilon}=\epsilon_1+i\epsilon_2$. The Brewster angle spectroscopy method determines the Brewster angle φ_B and the reflectivity at this angle $R_p|\varphi_B$ for p-polarized light. Therefore expressions are needed which correlate φ_B and $R_p|\varphi_B$ with ϵ_1 and ϵ_2. In the modeling procedure below, the optical behavior, i.e., the spectral dependence of ϵ_1 and ϵ_2, is approximated and the influence of a defect at a given energy on φ_B and $R_p|\varphi_B$ is calculated. Such an approach allows for later analysis of the experimental data.

In a first step, we simulate the optical properties of a semiconductor with an energy gap of 1.5 eV using the established superposition method of Lorentz oscillators[31]

$$\bar{\epsilon}=\epsilon_1-i\epsilon_2=\epsilon_\infty+\sum_k \frac{S_k}{\omega_k^2-\omega^2+i\omega\Gamma_k}, \quad (1)$$

with ω_k: frequencies of the absorbing centers; Γ_k: damping constants; s_k: oscillator strengths. The oscillator strengths are taken as a phenomenological measure for the contribution of matrix elements and joint density of states (JDOS) to the overall excitation and transition probability. Figure 2 shows ϵ_1, ϵ_2, φ_B, and $R_p|\varphi_B$ for a material with similar optical properties as CdTe. Due to its energy gap and available information on material properties, the simulated behavior can be compared below with the actual optical behavior of $CuInS_2$ whose optical properties in this energy range are rather unknown. The assumed data for ω_k, Γ_k, and s_k used to produce the spectra in Fig. 2 are given in Table II. $R_p|\varphi_B$ and φ_B are determined from ϵ_1 and ϵ_2 using

$$R_p=\frac{\sqrt{|\epsilon|^2-2\epsilon_1y^2+y^4}+|\epsilon|^2x^2-x(\sqrt{|\epsilon|^2-2\epsilon_1y^2+y^4}+y^2)\sqrt{2(\sqrt{|\epsilon|^2-2\epsilon_1y^2+y^4}+\epsilon_1-y^2)}}{\sqrt{|\epsilon|^2-2\epsilon_1y^2+y^4}+|\epsilon|^2x^2+x(\sqrt{|\epsilon|^2-2\epsilon_1y^2+y^4}+y^2)\sqrt{2(\sqrt{|\epsilon|^2-2\epsilon_1y^2+y^4}+\epsilon_1-y^2)}}, \quad (2)$$

$$\varphi_B=\arcsin\left[\sqrt{\frac{-|\epsilon|^2}{3(|\epsilon|^2+\epsilon_1)}\left[|\epsilon|^2-3+\cos\left(\frac{\chi}{3}+\frac{4\pi}{3}\right)\sqrt{|\epsilon|^4+6|\epsilon|^2+12\epsilon_1+9}\right]}\right], \quad (3)$$

with

$$\cos\chi=\frac{|\epsilon|^4|\epsilon|^8+9\epsilon^6+27|\epsilon|^4+18|\epsilon|^4\epsilon_1-27|\epsilon|^2+54|\epsilon|^2\epsilon_1+54\epsilon_1^2}{\sqrt{(|\epsilon|^4+6|\epsilon|^2+12\epsilon_1+9)^3}}.$$

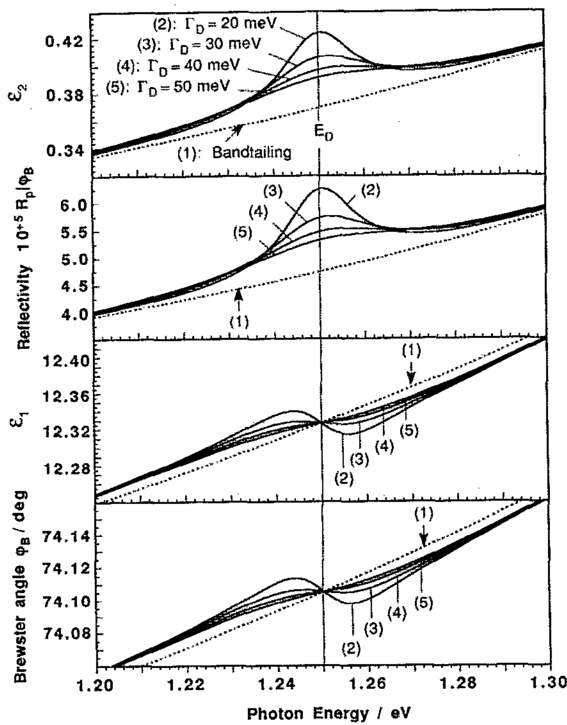

FIG. 4. Influence of a small defect oscillator with various damping constants and an assumed oscillator strength of $s_D=10^{-2}\ s_{Eg}$ within the band gap.

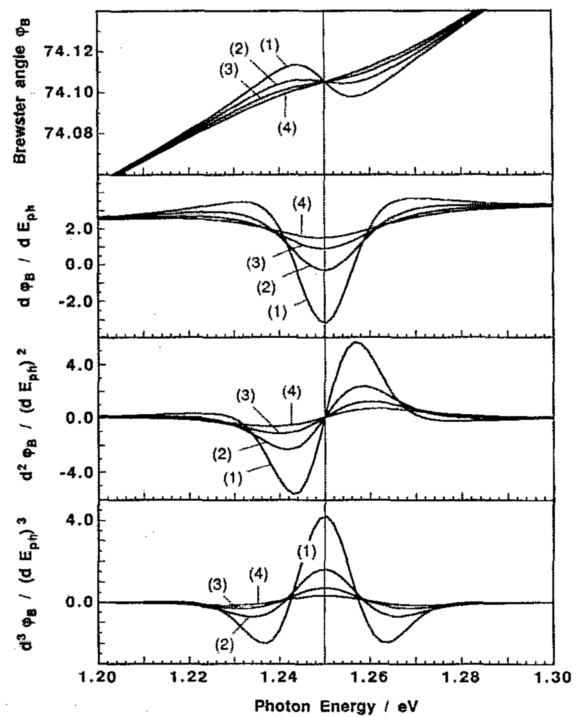

FIG. 5. Determination of the energetic defect position at 1.25 eV using the first, second, and third derivative of the Brewster angle φ_B. The variations of φ_B are taken from Fig. 4.

In Eqs. (2) and (3), $y=\sin\varphi$, $x=\cos\varphi$, and φ denotes the angle of incidence. Details are given in Appendix A and elsewhere.[23,32]

We now consider a defect energetically located well below the band gap energy and apply the formalism of Eq. (1) for its representation. In Fig. 3, a defect is assumed at $h\nu=1.25$ eV. The oscillator strength has been varied from $s_D=s_{Eg}(1)$ to $s_D=10^{-2}\ s_{Eg}(1)$. $s_{Eg}(1)$ denotes the oscillator strength of the main oscillator strength at 1.5 eV used to produce the optical properties shown in Fig. 2 (first parameter set in Table II). Also shown is the band tail from the onset of interband transitions. The figure shows that the spectral behavior of ϵ_2 is almost identical to the corresponding dependence of $R_p|\varphi_B$. Similarly, the behavior of ϵ_1 is reflected by the spectral changes of φ_B. Obviously, the reflectivity for p-polarized light at the Brewster angle is a measure for the absorptivity whereas the spectral behavior of the Brewster angle itself describes largely the refractory properties. The influence of the damping constant is displayed in Fig. 4 for the lowest assumed values of s_D in Fig. 3. The simulated data show that broadened structures are considerably more difficult to detect. This indicates that the method could gain additional sensitivity if measurements at low temperature are performed. The determination of the exact energetic position of a defect is of significant importance for the possible assignment of the structure to a specific point defect in the respective sample. Figures 3 and 4 show that the energetic position can be either determined by a maximum in $R_p|\varphi_B$ or by the inflection point of φ_B with photon energy. For very weak defect structures a comparably exact defect position identification can be obtained by using the definition $d^2\varphi_B/dE_{\mathrm{ph}}^2=0$ and $d^3\varphi_B/dE_{\mathrm{ph}}^3>0$. The corresponding graphic derivatives are displayed in Fig. 5. Therefore, experimental data from weak defects have to be processed for smoothing as described in the experimental section (see Appendix C). Taking into account the experimental limitations in the determination of reflectivity near the Brewster angle (see Appendix B), it seems useful to determine small defect induced changes from the occurring variations in the Brewster angle spectra.

In Fig. 6, three defects are assumed with different damping constants as parameters. Interestingly, the differences in Γ_D are quite visible in ϵ_2 and $R_p|\varphi_B$, but are not so well resolved in ϵ_1 and φ_B. It should also be noted that the superposition of defect structures which are energetically close to each other can result in errors in the identification of the defect energy position. This situation is not yet reached in the simulation shown in Fig. 6 but would occur for larger oscillator strength thus necessitating a deconvolution procedure. Also the energetic position of defects located in an energy range where the band tails are steep is shifted due to superposition and asymmetric defect structures are expected.

The model also allows correlations to the spectral behavior of ϵ_1 and ϵ_2 and to predict the corresponding

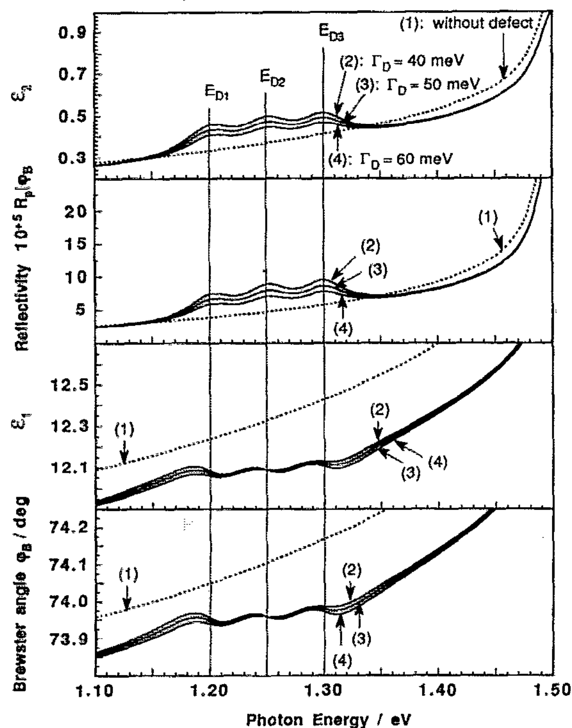

FIG. 6. Influence of three energetically distinguishable defect oscillators with various damping constants energetically located well below the band gap energy.

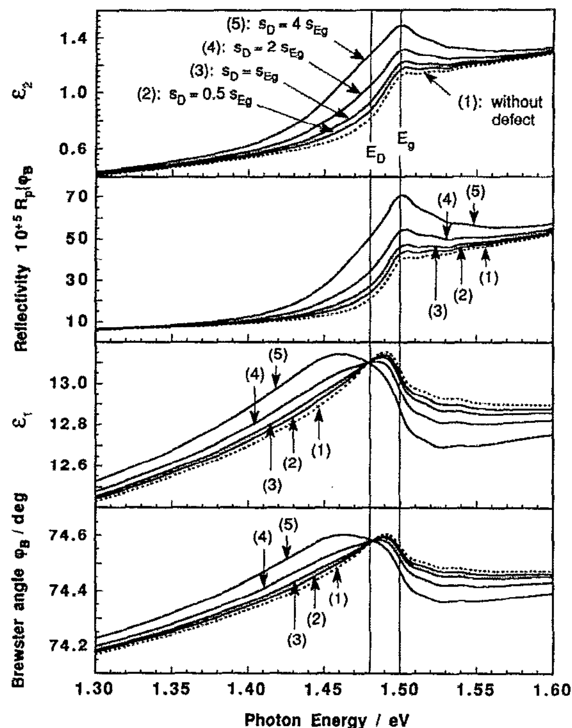

FIG. 7. Influence of defect oscillators with various oscillator strengths near the band gap energy on ϵ_2, R_p, ϵ_1, and φ_B. The defect oscillator energy is assumed 20 meV below the band gap energy with a damping constant Γ_D=50 meV.

changes in φ_B and $R_p|\varphi_B$ for a defect at $E_{\rm Ph}$=1.48 eV, just below the band edge at 1.50 eV (Fig. 7). Different oscillator strengths as indicated in the figure have been assumed and it can be seen that a pronounced change in the band tail absorptivity (ϵ_2) is found as well as an inflection point for ϵ_1 at the defect energy. Therefore it should in principle be possible to analyze shallow defects at least in selected cases as, for instance, in highly doped semiconductors which are otherwise insensitive to electrical field modulation techniques due to their high capacitance.

IV. RESULTS AND DISCUSSION

A. Deep level analysis

The spectral changes of φ_B and its second derivative are displayed for GaAs in Figs. 8 and 9. For the slightly n-type, nominally undoped material, the data in Fig. 8 reveal a series of defect positions as indicated by the arrows. Defects at 0.79, 0.83, 0.92, 0.99, and possibly 1.20 eV are observed. For a n-type sample, doped with Sn, the measured Brewster angle spectrum and the second derivative spectrum are plotted in Fig. 9. The processing of these rather noisy data [Fig. 9(a)] is described as an example for the evaluation procedure and the formation of derivatives in Appendix C. The second derivative spectrum is shown at a higher spectral reduction compared to Fig. 8 and exhibits various pronounced features. The defect positions at 0.79, 0.84, 0.91, and possibly at 0.99 eV are consistent with those of the undoped sample (Fig. 8) within the error margin. Additional structure at 0.81, 0.87, 0.96, and 1.04 eV is found in Fig. 9.

A comparison of the defect positions found for the nominally undoped sample with literature data shows that the energetic positions at 0.79, 0.99, and 1.20 eV (Fig. 8) might be attributed to the EL2 defect family.[20,33,34] This intensively studied defect class is frequently attributed to a $(As_{Ga})_n$-X variety[35] where n is the number of centers and X defines the six basic lattice defects.[35-37] Other models of defect structures exhibiting As on a Ga position exist[33] showing that the common feature is the deep donor property of the EL2 ground state occupied with two electrons.

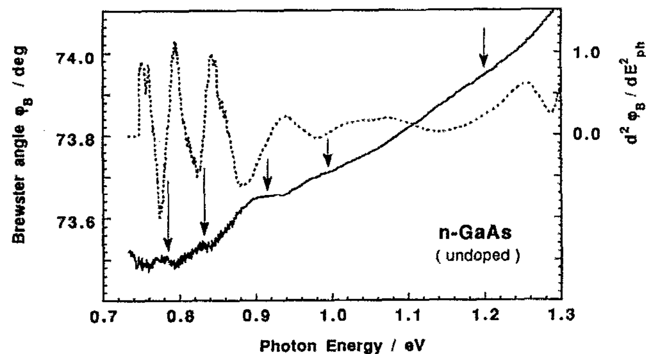

FIG. 8. Spectral dependence of the Brewster angle φ_B and its second derivative for undoped n-GaAs.

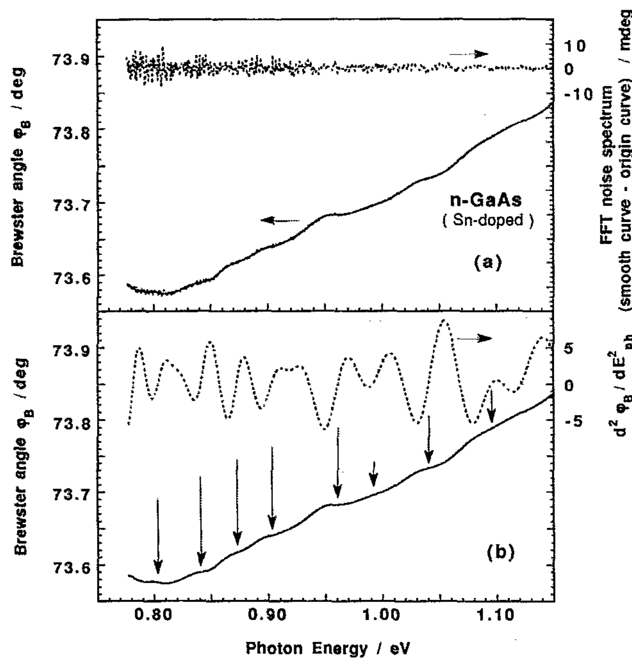

FIG. 9. Spectral dependence of (a) the Brewster angle φ_B for Sn-doped n-GaAs and (b) its second derivative; also shown is a noise spectrum (see Appendix C).

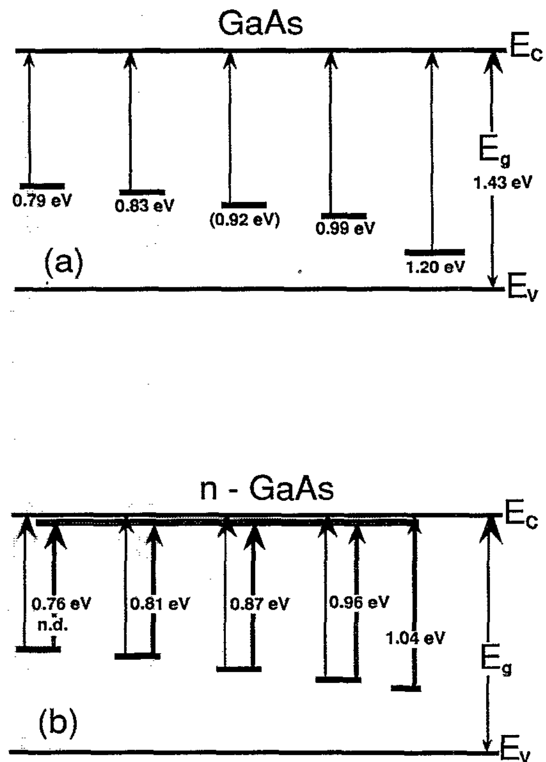

FIG. 10. (a) Schematic energy level diagram for (a) undoped GaAs and (b) doped n-GaAs.

This state has been observed in the photon energy range between 0.76 eV and is tabulated at 0.79 eV.[38] For high pressure Bridgman growth, a value of 0.81 eV is reported.[39] Since the hitherto reported data have been obtained at low temperature, the change of the GaAs energy gap with temperature T has in principle to be considered when comparison with our room temperature measurements is made. The data spread at low temperature, however, is of the same size as $\Delta E_g(T)$ and we therefore tentatively assign the signal at 0.79 eV to the $EL2^{0/+}$ defect. The signal at $h\nu = 0.99$ eV fits very well with data on the oxidized defect $EL2^{+/++}$ which are reported to lie ≈ 1.00 eV below the conduction band edge.[20] The signal at 1.20 eV might be very tentatively attributed to the so-called metastable state EL2* which has not been observed directly so far but has been postulated due to the quenching of the EL2 defect signal at low temperature.[8,33,35,40] The transition EL2→EL2* occurs at about 1.20 eV and leads to a disappearance of the EL2 signal. The signal can be recovered by annealing to $T = 140$ K. In the present room temperature experiment the visibility of the transition might be due to the competition between quenching of the defect by optical excitation and thermal healing at room temperature. This argumentation, however, is quite speculative as we did not specifically study this phenomenon but intend to demonstrate the capacity of Brewster angle spectroscopy (BAS) to identify defects at ambient temperature. The usual concentration of EL2 centers in GaAs ranges between $5 \cdot 10^{15}$ cm^{-3} and $2 \cdot 10^{16}$ cm^{-3} in Czochralski grown material.[41] Assuming similar defect densities in our high pressure Bridgman grown material, this indicates already the exceptional sensitivity of the method. The features at 0.83 and 0.92 eV are attributed to the EL0 and HL8 defect using tabulated data.[38]

The observation of four additional features in Sn-doped n-GaAs might be explained on the basis of the already discussed defect levels. Assuming an energetic distribution of the Sn dopant of 20–50 meV below E_c at room temperature [see Fig. 10(b)], the additional structure at 0.96, 0.87, and 0.81 eV can be explained by transitions from deep levels to partly empty shallow donors. The line at 1.04 eV cannot be easily explained on this basis. It might be attributed to the faint feature at 1.07 eV in Fig. 8 or result from a change in the defect distribution due to the doping. Figure 10 summarizes the results schematically. The broader level for the dopant is indicated below the conduction band minimum in the lower part of the figure.

Figure 11(b) shows the spectral Brewster angle dependence and the second derivative for nominally undoped slightly n-type InP. The noise analysis of the measured data are shown in Fig. 11(a). A series of features at $h\nu = 0.78$, 0.83, 0.87, 0.91, 1.11, 1.20, and 1.28 eV is observed. Some of the features are marked by a dashed arrow to indicate less pronounced signals. The assignment to tabulated literature values is possible[42] but the information concerning these defects (B, $E1$, R, $E2$, C, T, $E4$, $E3$, $E8$, F, and unidentified, respectively) is rather scarce compared to GaAs. We are therefore not going into details at this point. The Brewster angle spectrum for Zn-doped p-type InP is displayed in Fig. 12 including the second derivative. It turns out that the difference to the spectrum in Fig. 11 is an

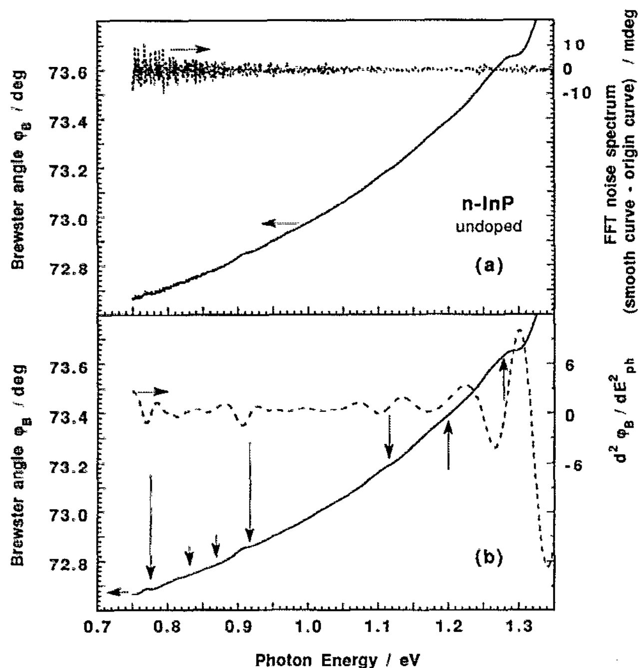

FIG. 11. (a) Spectral dependence of the Brewster angle φ_B and (b) its second derivative of φ_B for undoped n-InP; also shown is a noise spectrum (see Appendix C).

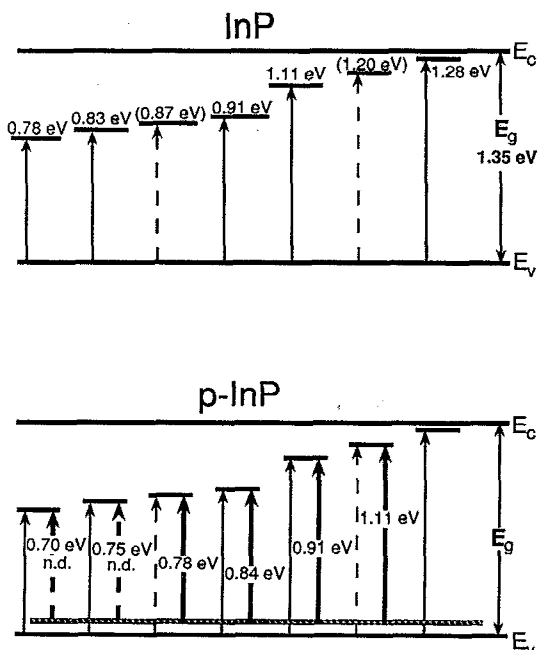

FIG. 13. (a) schematic energy diagram for undoped InP and (b) energy diagram for p-InP.

additional line occurring at 1.02 eV and the missing line at 1.20 eV in the p-type sample. Zn is known to have an energetic position of $E_a = E_v + 0.05$ eV in InP.[43] Assuming an energetic range of 50–80 meV for the shallow acceptor at room temperature it is possible to assign the data for the undoped and Zn-doped sample to transitions from the top of the valence band and from partially filled Zn acceptor levels to deep acceptors as shown in Fig. 13. Since some of the defect levels are energetically separated by about 80 meV (see for instance 1.28−1.20 eV, 1.20−1.11 eV, 0.91 −0.83 eV, 0.87−0.78 eV in the undoped sample) the incorporation of a level located energetically approximately 80 meV above E_v does not result in a series of new structure. The new structure in p-InP at 1.03 eV is attributed to a transition from E_a (Zn) to the defect at 1.11 eV in the undoped sample and this feature does also fit well in this picture. The possible transitions at 0.75 and 0.70 eV into the levels at $E_v + 0.83$ eV and $E_v + 0.78$ eV (Fig. 11) are below the accessible spectral range. The origin of the disappearance of the signal at 1.20 eV has not yet been clarified.

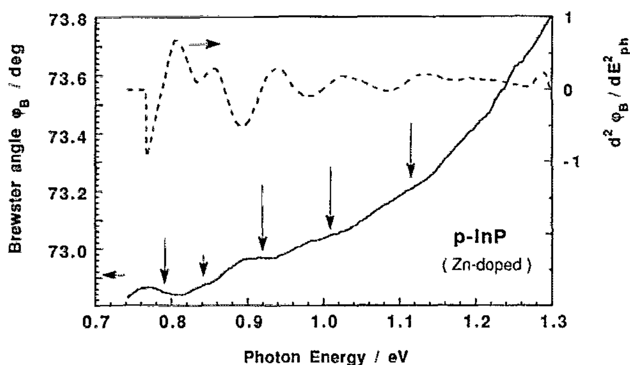

FIG. 12. Spectral dependence of the Brewster angle φ_B and its second derivative of φ_B for Zn-doped p-InP.

The identification of absorbing deep levels by maxima in R_p at angles close to φ_B is shown in Fig. 14 for a $CuInS_2$ crystal. Upon increasing the angle of incidence φ towards $\varphi_B = 71.247°$, structure develops in the subband gap region. By changing φ from 50°, 60° to 65° and then 70°, the defect structure increases superlinearly when comparing the change in defect structure from $\varphi = 50°$ to 60°. Also the absolute reflectivity values drop by a factor of about 20. It is important to verify that the subband gap structure does not depend on the angle of incidence to exclude internal multiple reflections. The defects identified by the assignment at the bottom of Fig. 14 are located at 0.80, 0.90, 0.94, 1.03, 1.13, 1.20, and 1.26 eV.

From photoluminescence data, the most common defects in $CuInS_2$ are the acceptor states V_{Cu}, S_i, and the donor levels due to V_S at $E_c - 0.035$ eV, In_i at $E_c - 0.070$ eV and In_{Cu} at $E_c - 0.110$ eV.[28,30,44–48] Using these values we can correlate the observed subband gap features in Fig. 14 to transitions into these partly empty donors of the moderately n-type $CuInS_2$ sample (grown with In and sulphur excess) if two hitherto not observed defects are assumed at $E_V + 0.350$ eV (D_1) and at $E_V + 0.625$ eV (D_2). The data then fit excellently into the energy scheme shown in Fig. 15. The missing observation of the D_1 and D_2 level in photoluminescence is presumably due to nonradiative recombination via those levels, possibly even at low temperatures. The assignment of the D_1 and D_2 level to specific

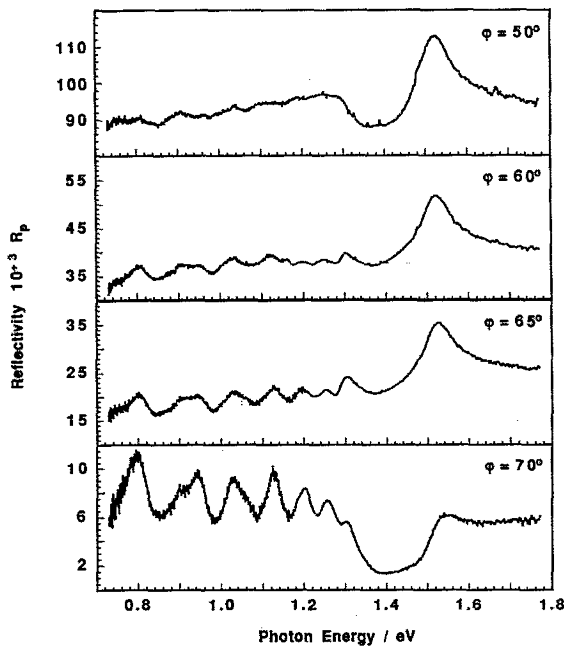

FIG. 14. The measured reflectivity R_p for various angles of incidence (φ=50°, 60°, 65°, and 70°) for n-$CuInS_2$ grown with In and sulphur excess.

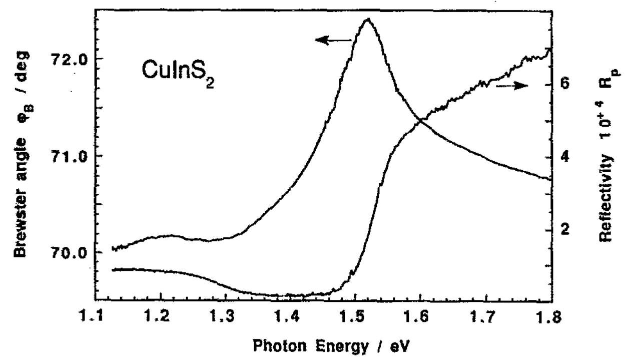

FIG. 16. Spectral dependence of the Brewster angle φ_B and reflectivity $R_p|\varphi_B$ for intrinsic as-grown $CuInS_2$.

point defects is not possible at present and needs further analysis of such samples under varying conditioning experiments.[32]

B. Shallow defect levels

The influence of shallow defects on the Brewster angle and the reflectivity $R_p|\varphi_B$ has been shown in Fig. 7. In particular, for high oscillator strength ($S_D = 4S_{E_g}$, curve 5 in Fig. 7) an inflection of φ_B at the defect level and at the band gap energy occurs. Figure 16 shows φ_B and $R_p|\varphi_B$ spectra of a lamellae $CuInS_2$ sample with high crystallinity as evidenced by reflection high-energy electron diffraction (RHEED) and x-ray diffraction (XRD).[29,49] The measured data correspond quite well to the model spectra (curves 1–3 in Fig. 7) indicating a comparably low shallow defect concentration. These samples are highly stoichiometric and show a high electrical resistivity. In contrast, Fig. 17 shows the corresponding data for a sample grown with sulphur excess at elevated pressure.[30,32] The sample is p-type conducting and it can be seen that the spectral dependence of φ_B resembles the data given in Fig. 7 for a high oscillator strength, simulating a large number of defects. An inflection point at the defect energy as shown for φ_B in curve 5 in Fig. 7 is not observed in the experimental data possibly because of a considerable energetic spread of various defects which overlap energetically. The experimental data actually resemble better those of curve 4 in Fig. 7 indicating an intermediate concentration of shallow defects. Since the sample has been grown with sulphur excess, the assumption of S_i sites is reasonable. From the data in Fig. 15, such a level would be located at E_V+0.018 eV. The comparison of Fig. 7, curve 4 for φ_B and the corresponding curve in Fig. 17 locate the defect position at about 1.4 eV. This is a reasonable agreement assuming an energy gap of 1.55 eV (see Fig. 15),[48,50] which leads to a defect position of E_V+0.015 eV.

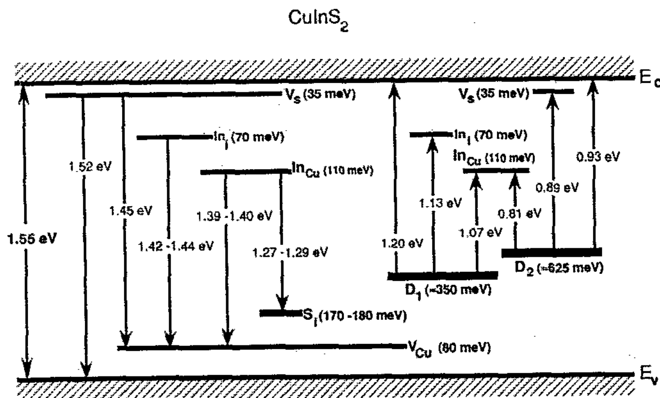

FIG. 15. Energy level diagram for $CuInS_2$. The defect levels are obtained using photoluminescence and BAS data.

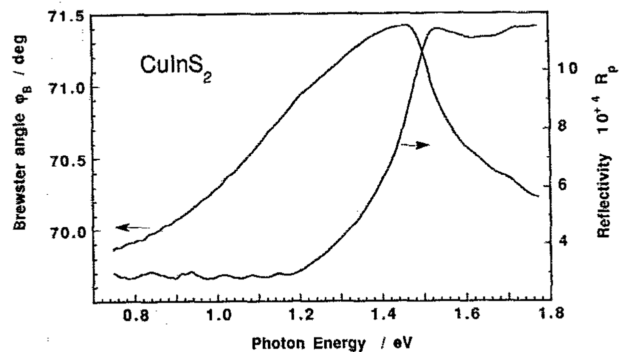

FIG. 17. The measured spectral dependence of the Brewster angle φ_B and reflectivity $R_p|\varphi_B$ for $CuInS_2$ grown with excess sulphur.

V. CONCLUSIONS

Brewster angle spectroscopy (BAS) allows the identification of defects at room temperature without electrical contacting. The sensitivity of the method results from the extinction condition for reflection of p-polarized light at the Brewster angle and the sensitive changes of the Brewster angle upon additional absorption in the energy range below semiconductor band gaps. In GaAs and InP, defects have been identified by BAS in accordance with literature data. The changes in the BAS signals from doped GaAs and InP samples could be mostly attributed to additional transitions between defects and shallow donor and acceptor states. In $CuInS_2$ transitions involving the donor levels well known from photoluminescence experiments could be observed. The data led to the postulation of two additional hitherto unknown deep defects in $CuInS_2$. The identificationof shallow acceptors in $CuInS_2$ samples grown with slight sulphur excess was possible by comparison with model spectra. The energetic comparison led to the postulation of interstitial sulphur located at $E_V+0.015$ eV.

ACKNOWLEDGMENT

We would like to thank J. Grzanna for noise analysis calculations and computing.

APPENDIX A

For comparative purposes, it appears meaningful to transform the measured data of φ_B and $R_p|\varphi_B$ into the well-known optical constants. The interrelation between the measured Brewster angle φ_B and the reflectivity $R_p|\varphi_B$ with the optical constants ϵ_1 and ϵ_2 is given by

$$\epsilon_1=\frac{|\epsilon|^2}{2\sin\varphi_B^2}\left[1+2\cos^2\varphi_B-|\epsilon|^2\frac{\cos^4\varphi_B}{\sin^4\varphi_B}\right]$$

and

$$\epsilon_2=\sqrt{|\epsilon|^2-\epsilon_1^2}, \tag{A1}$$

$|\epsilon|^2$ too, is a function of φ_B and $R_p|\varphi_B$.

The refractory index n and the absorption coefficient α are determined from ϵ_1 and ϵ_2 by

$$n=\sqrt{\frac{1}{2}(|\epsilon|+\epsilon_1)}$$

and

$$\alpha=\frac{2\pi}{\lambda}\sqrt{\frac{1}{2}(|\epsilon|-\epsilon_1)}, \tag{A2}$$

where λ denotes the wavelength of the light.

The development of the functional dependence $(\epsilon_1,\epsilon_2)=F(\varphi_B,R_p|\varphi_B)$ is briefly shown here:

The equation for the reflectivity R_p is developed from the complex Fresnel equation r_p where the complex dielectric function of the ambient=1 and that of the substrate ϵ

$$r_p=\frac{\epsilon\cos\varphi-\sqrt{\epsilon-\sin^2\varphi}}{\epsilon\cos\varphi+\sqrt{\epsilon-\sin^2\varphi}}, \tag{A3}$$

and

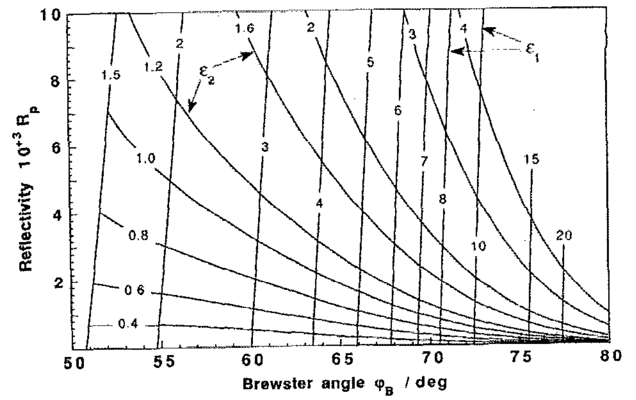

FIG. 18. Sensitivity card for the Brewster angle φ_B and the reflectivity R_p at that angle.

$$R_p=r_pr_p^*=\frac{\mu+|\epsilon|^2\cos^2\varphi-\cos\varphi(\mu+\sin^2\varphi)\sqrt{2(\mu+\kappa)}}{\mu+|\epsilon|^2\cos^2\varphi+\cos\varphi(\mu+\sin^2\varphi)\sqrt{2(\mu+\kappa)}}, \tag{A4}$$

with

$$\mu^2=|\epsilon|^2-2\epsilon_1\sin^2\varphi+\sin^4\varphi$$

and

$$\kappa=\epsilon_1-\sin^2\varphi.$$

The analytical expression for the Brewster angle can be developed from the reflectivity minima R_p, by solving a third order equation.[23,32] The Brewster angle for a complex dielectric function ϵ is therefore given by

$$\varphi_B=\arcsin\left[\sqrt{\frac{-|\epsilon|^2}{3(|\epsilon|^2+\epsilon_1)}\left[|\epsilon|^2-3+\cos\left(\frac{\chi}{3}+\frac{4\pi}{3}\right)\sqrt{b}\right]}\right], \tag{A5}$$

with

$$\cos\chi=\frac{|\epsilon|^4c}{\sqrt{b^3}};\quad b=|\epsilon|^4+6|\epsilon|^2+12\epsilon_1+9$$

$$c=|\epsilon|^8+9\epsilon^6+27|\epsilon|^4+18|\epsilon|^4\epsilon_1-27|\epsilon|^2+54|\epsilon|^2\epsilon_1+54\epsilon_1^2. \tag{A6}$$

For a minute imaginary part of the dielectric function ϵ, Eq. (3) reduces to the well-known relation $\varphi_B=\arctan\sqrt{\epsilon}$.

Using the experimental parameters Brewster angle φ_B and the reflectivity $R_p|\varphi_B$ the method has a similar sensitivity using the ratio $(R_p/R_s)|\varphi_B$, presented by Humphreys-Owen.[19] Figure 18 shows the sensitivity card of the method used here. In this card the two measured quantities $R_p|\varphi_B$ and the Brewster angle φ_B form the axes, in which families of iso-ϵ_1 and iso-ϵ_2 contours are drawn. The sensitivity can be estimated from the spaces between the curves for a given scale. Large spacing means high sensitivity and vice versa.

1. Optical constants derived from Brewster angle φ_B and reflectivity $R_p|\varphi_B$

Equation (A4) can be rewritten in the form[32]

$$R_P=\frac{r-s}{r+s}, \tag{A7}$$

where $r=\mu+|\epsilon|^2x^2$; $s=x(\mu+y^2)\sqrt{2\mu+\kappa}$; $x=\cos\varphi$ and $y=\sin\varphi$. Let $L_P=\frac{s}{r}=\frac{1-R_p}{1+R_p}$, and in the expression for L_p^2 with

$$L_p^2=\frac{x^2(\mu+y^2)^2(2\mu+\kappa)}{(\mu+|\epsilon|^2x^2)^2}, \tag{A8}$$

substituted for μ and μ^2 using the minima condition for the Brewster angle

$$\mu=\mu_B=\frac{|\epsilon|x_B^2-y_B^2}{y_B^2}. \tag{A9}$$

Rearranging (A8) with respect to (A9) yields an analytical expression which is of fourth order in $|\epsilon|^2$.

$$|\epsilon|^8-|\epsilon|^6\frac{y^4(4x^4+1)}{x^4}+|\epsilon|^4\frac{y^6[4x^2y^2+L_p^2(y^2+1)^2]}{x^6}$$
$$-|\epsilon|^2\frac{2y^{10}L_p^2(y^2+1)}{x^8}+\frac{y^{14}L_p^2}{x^{10}}=0. \tag{A10}$$

Substituting $b=|\epsilon|^2-\frac{y^4(4x^4+1)}{4x^4}$, (A10) can be written in the form

$$b^4+ub^2+vb+w=0, \tag{A11}$$

where

$$u=\frac{y^6}{x^6}[4y^2x^2+L_p^2(y^2+1)^2]-\frac{3y^8}{8x^8}(4x^2+1),$$

$$v=\frac{-2y^{10}}{x^8}L_p^2(y^2+1)-\frac{y^{12}}{8x^{12}}(4x^2+1)^3,$$
$$+\frac{y^{10}}{2x^{10}}(4x^2+1)(4y^2x^2+L_p^2(y^2+1)^2)$$

$$w=\frac{y^{14}}{x^{10}}L_p^2+\frac{3y^{16}}{256x^{16}}(4x^2+1)^4+\frac{y^{14}}{16x^{14}}(4x^2+1)^2$$
$$\times(4y^2x^2+L_p^2(y^2+1)^2)-\frac{y^{14}L_p^2}{2x^{12}}(4x^2+1)(y^2+1).$$

The general solution can be written as

$$\epsilon_1=\frac{|\epsilon|^2}{2\sin^2\varphi_B}\left[1+2\cos\varphi_B^2-|\epsilon|^2\frac{\cos^4\varphi_B}{\sin^4\varphi_B}\right]$$

and

$$\epsilon_2=\sqrt{|\epsilon|^2-\epsilon_1^2} \tag{A12}$$

with

$$|\epsilon|=\sqrt{\frac{1}{2}\{\sqrt{z_1}+\sqrt{z_2+z_3+2\sqrt{z_2z_3}}\}+\frac{\cos^4\varphi_B}{\sin^4\varphi_B}(1+4\cos^2\varphi_B)}, \tag{A13}$$

z_1, z_2, and z_3 are solutions of the cubic equation

$$z^3+2uz^2+(u^2-4w)z+v^2=0, \tag{A14}$$

and determined by

$$p=(u^2-4w)-\frac{4}{3}u^2;\quad q=\frac{16}{27}u^3-\frac{2}{3}u(u^2-4w)-v^2;$$

$$D=\left(\frac{p}{3}\right)^3+\left(\frac{q}{2}\right)^2 \quad\text{and}\quad R=\text{sign}(q)\sqrt{\frac{|p|}{3}}.$$

Case I ($p<0$ and $D\leqslant 0$): the solutions are

$$z_1=-2R\cos\left[\frac{1}{3}\arccos\left(\frac{q}{2R^3}\right)\right]-\frac{2u}{3},$$

$$z_2=-2R\cos\left[\frac{1}{3}\arccos\left(\frac{q}{2R^3}\right)+\frac{2\pi}{3}\right]-\frac{2u}{3},$$

$$z_3=-2R\cos\left[\frac{1}{3}\arccos\left(\frac{q}{2R^3}\right)+\frac{4\pi}{3}\right]-\frac{2u}{3}.$$

Case II ($p<0$ and $D>0$):

$$z_1=-2R\cosh\left[\frac{1}{3}\text{arccosh}\left(\frac{q}{2R^3}\right)\right]-\frac{2u}{3},$$

$$z_2=R\cosh\left[\frac{1}{3}\text{arccosh}\left(\frac{q}{2R^3}\right)\right]-\frac{2u}{3}$$
$$+i\sqrt{3}R\sinh\left[\frac{1}{3}\text{arccosh}\left(\frac{q}{2R^3}\right)\right],$$

and $z_3=z_2^*$ (*: complex conjugated).

Case III ($p>0$):

$$z_1=-2R\sinh\left[\frac{1}{3}\text{arcsinh}\left(\frac{q}{2R^3}\right)\right]-\frac{2u}{3},$$

$$z_2=R\sinh\left[\frac{1}{3}\text{arcsinh}\left(\frac{q}{2R^3}\right)\right]-\frac{2u}{3}$$
$$+i\sqrt{3}R\cosh\left[\frac{1}{3}\text{arcsinh}\left(\frac{q}{2R^3}\right)\right],$$

and

$$z_3=z_2^*.$$

Figure 19 shows a contour plot of ϵ_2 vs ϵ_1 for various values φ_B and $R_p|\varphi_B$ calculated according to (A12). The graph shows the interrelations between the measured values and the optical constants for typical semiconductors like GaAs, InP, or CdTe in weak absorption regions.

APPENDIX B. EXPERIMENTAL LIMITATIONS IN THE DETERMINATION OF φ_B AND $R_p|\varphi_B$

The determination of reflectivity near the Brewster angle is limited through the occurring divergence and depolarization of the parallel polarized light of incidence. The

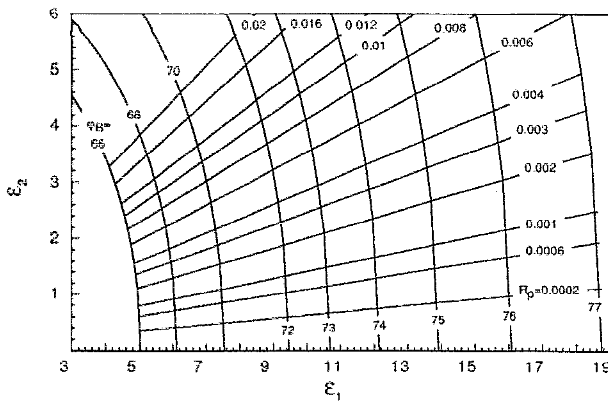

FIG. 19. Families of iso- $R_p|\varphi_B$ and iso-φ_B contours in the $\epsilon_1-\epsilon_2$ plane. $R_p|\varphi_B$ is the reflectivity at the Brewster angle φ_B for light, polarized parallel to the plane of incidence with assumed values in low absorption regions. φ_B is the Brewster angle with assumed values from 66° upto 77°. This nomogram represents a part of the analytical solution of Eq. (15).

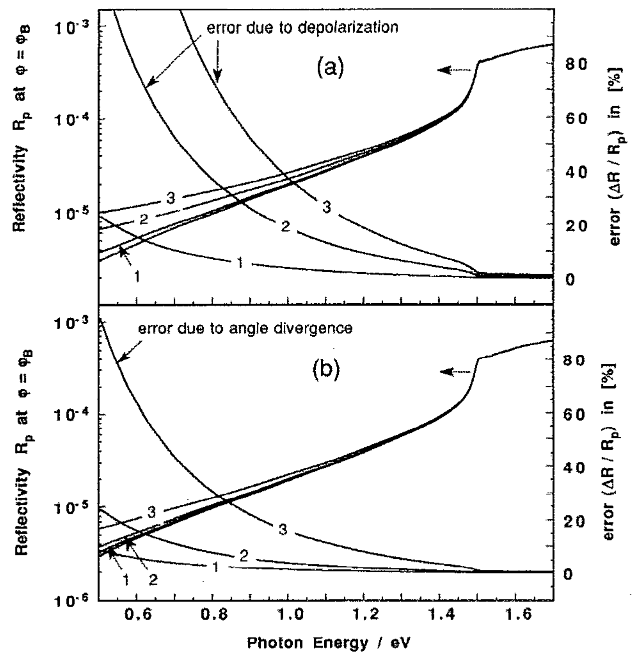

FIG. 20. Error calculations due to angle divergence and depolarization of the beam of incidence. (a) occurring errors in the reflectivity through assumed depolarization ratios (R_s to R_p) curve 1: 1×10^{-6}; curve 2: 5×10^{-6}, and curve 3: 1×10^{-5}. (b) occurring errors in the determination of reflectivity for assumed angle divergences curve 1: 0.06°; curve 2: 0.1°, and curve 3: 0.2°.

depolarization ratio (R_s/R_p) of a Glan Thompsen prism is better than 10^{-6}. The error in reflectivity due to depolarization can therefore be estimated to be 10^{-6} multiplied with the reflectivity R_s of the substrate.

Estimation of the error induced by the angle divergence of the light beam can be analyzed as follows: around the Brewster angle the reflectivity can be expressed as

$$R(\varphi)=R|_{\varphi_B}+\frac{\Delta R}{\theta^2}(\varphi-\varphi_B)^2. \tag{B1}$$

Here φ is the angle of incidence, φ_B the Brewster angle of the substrate, $R|\varphi_B$ the reflectivity at this angle, and ΔR the difference between $R|\varphi_{B-\theta}$ and $R|\varphi_B$. The interval of the angle, defined by 2θ, lies in the order of 0.2° up to over 4°, depending on the absorption of the material. The experimentally resolved reflectivity $\bar{R}$ at the Brewster angle can be calculated as

$$\bar{R}|_{\varphi_B}=\frac{1}{2\alpha}\int_{\varphi_B-\alpha}^{\varphi_B+\alpha}R(\varphi)d\varphi$$

$$=R|_{\varphi_B}+\frac{\Delta R\alpha^2}{3\theta^2}=R|_{\varphi_B}+\frac{|R|_{\varphi_{B-\alpha}}-R|_{\varphi_B}|}{3}. \tag{B2}$$

Here, 2α is the interval of angle divergence with $\alpha\leqslant\theta$. For any other angle of incidence φ inside the interval $[\varphi_B\pm\theta]$ the experimentally resolved reflectivity is given as

$$\bar{R}|_{\varphi_x}=R|_{\varphi_B}+\frac{\Delta R}{6\theta^2\alpha}[(\varphi_{x+\alpha}-\varphi_B)^3+(\varphi_{x-\alpha}-\varphi_B)^3], \tag{B3}$$

where $\varphi_{x\pm\alpha}$ lies inside the angle interval $[\varphi_B\pm\theta]$.

For any angle of incidence φ outside of the interval $[\varphi_B\pm\theta]$ the reflectivity can be estimated through a linear function for angle divergences in the order of 0.2° or less. Linear function approximation, however, means that no significant error occurs during a distribution of symmetrical angle divergence. In a first approach, a distribution of linear angle divergence was assumed.

The resulting errors with assumed experimental limitations in the angle divergence and depolarization are shown in Fig. 20 (the ideal reflection behavior at the Brewster angle is taken from the optical constants, shown in Fig. 2). Figure 20(a) shows the errors in the determination of reflectivity through depolarization. Figure 20(b) shows the occurring errors by different assumed divergences in the beam of incidence. For an angle divergence greater than 1 mrad, a large error in the determination of reflectivities below 10^{-5} occurs.

APPENDIX C. DATA HANDLING

To determine the first and second derivative of the measured data two different algorithms were applied. At first, a compensation parabola method in the form of

$$\hat{y}_{x_i}=ax_i^2+bx_i+c, \tag{C1}$$

was used.[26]

The data interval $[y_{x-N/2},\ldots,y_{x+N/2}]$ around the data point y_{xi} was approximated through the normal equation

$$cN+b[x]+a[x^2]=[y]$$
$$c[x]+b[x^2]+a[x^3]=[xy]$$
$$c[x^2]+b[x^3]+a[x^4]=[x^2y], \tag{C2}$$

with $[x]=\Sigma_k x_k$ and $[y]=\Sigma_k y_{(x_k)}$, where k varies from $(-N/2)$ to $(+N/2)$.

By solving the normal Eq. (C2), the constants a, b, and c can be revealed in respect of the chosen interval

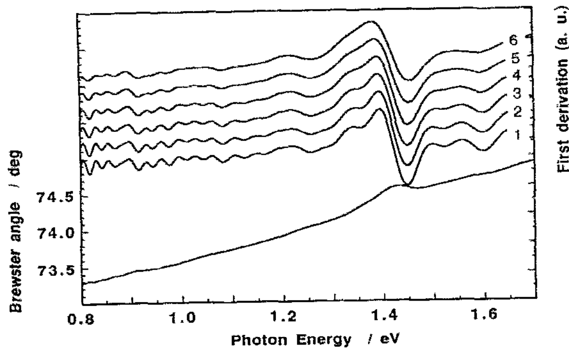

FIG. 21. Influence of the chosen length of interval N to the first derivative shown on p-GaAs spectrum (curve 1: 10; curve 2: 20; curve 3: 30; curve 4: 40; curve 5: 50; and curve 6: 60 data points).

$[y_{x-N/2},...,y_{x+N/2}]$ with $N+1$ data points. The length of the interval N has to be chosen in such a way that the condition

$$\frac{\Delta(\Delta y_{(x_k)}/\Delta x_k)}{x_{i+2}-x_i}=\text{constant}, \quad \text{(C3)}$$

is fulfilled (equal to: second derivative = constant).

The second derivative is then given as

$$f''_{(x_i)}=2a, \quad \text{(C4)}$$

the first derivative as

$$f'_{(x_i)}=2ax_i+b, \quad \text{(C5)}$$

and the approximated function value as

$$f_{(x_i)}=c+x_i f'_{(x_i)}-\frac{1}{2}x_i^2 f''_{(x_i)}. \quad \text{(C6)}$$

The quality of approximation by the compensation parabola method can be shown by comparing the calculated function values with the measured data. To compare the resolved derivations [(C4) and (C5)], a second algorithm was used. The algorithm is based on the Snyder algorithm[27] to determine the occurring minima/maxima positions in a given data range. The derivation of a data range can be determined by

$$f'_{(x_i)}=\sum_k f_{(x_{k-N/2})}h_{(x_{k-N/2})}; \quad k\in[0,N], \quad \text{(C7)}$$

where

$$h_{(x_{k-N/2})}=\begin{cases}-1:k\in[0,N/2) \\ 0:k=N/2 \\ +1:k\in(N/2,N],\end{cases} \quad \text{(C8)}$$

with $N\geqslant 1$.

By choosing N greater than 1 a slightly smoothing effect in the derivation occurs. For determination of the minima/maxima position in the spectra, this algorithm is much quicker compared to the parabola approximation method. But this algorithm cannot be used to determine

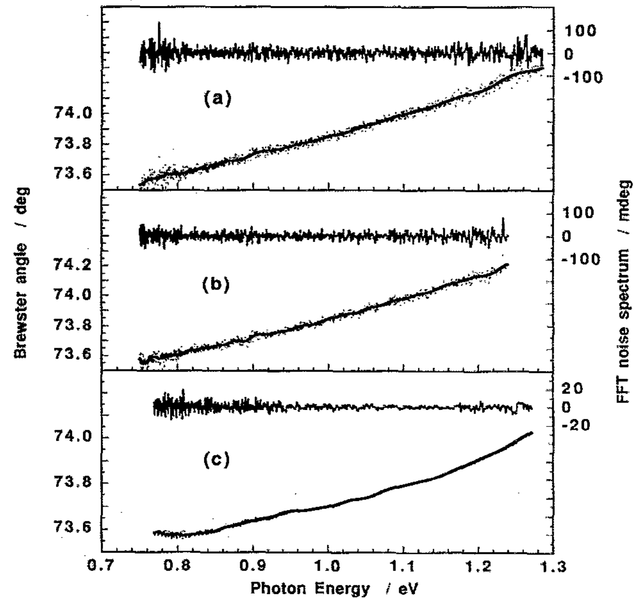

FIG. 22. Noise analysis of a measured Brewster angle spectra with different used step width. (a,b,c) spectra with angular step widths of 0.1°, 0.05°, and 0.02°, respectively.

the reflection minimum, which was revealed from the measured intensity in a symmetrically angular range around the Brewster angle.

The influence of the chosen length of interval N due to determine the first and second derivative is shown in Fig. 21.

Noise analysis was applied, using a fast Fourier algorithm.[51,52] The cutoff frequency window was revealed through the related power spectrum. Figure 22 shows as example the measured Brewster angle spectrum, the fast Fourier transform (FFT) smoothed spectrum and the filtered noise spectrum. It can be shown, that the statistically occurring errors in the determination of the Brewster angle lie in the order of the used angle step width. Typically, step widths of 0.01°–0.03° with angular ranges of 1°–5° were used, to determine the position of the Brewster angle.

[1] D. I. Desnica, J. Electron. Mater. **21**, 463 (1992).
[2] U. V. Desnica, D. I. Desnica, and B. Santic, Appl. Phys. Lett. **58**, 278 (1991).
[3] S. Duenas, E. Castán, A. d. Dios, L. Bailón, J. Barbolla, and A. Pérez, J. Appl. Phys. **67**, 6309 (1990).
[4] W. R. Buchwald, G. J. Gerardi, E. H. Poindexter, N. M. Johnson, H. G. Grimmeiss, and D. J. Keeble, Phys. Rev. B **40**, 2940 (1989).
[5] S. Makram-Ebeid and P. Boher, Rev. Phys. Appl. **23**, 847 (1988).
[6] J. Schneider, Mater. Res. Soc. Symp. Proc. **14**, 225 (1983).
[7] E. G. Bylander, C. W. Myles, and Y.-T. Shen, J. Appl. Phys. **67**, 7351 (1990).
[8] M. Kaminska, Rev. Phys. Appl. **23**, 793 (1988).
[9] D. Bimberg, H. Münzel, A. Steckenborn, and J. Christen, Phys. Rev. B **31**, 7788 (1985).
[10] R. Haak, C. Ogden, and D. Tench, J. Electrochem. Soc. **129**, 891 (1982).
[11] R. Haak and D. Tench, J. Electrochem. Soc. **131**, 275 (1984).
[12] B. Dischler and U. Kaufmann, Rev. Phys. Appl. **23**, 779 (1988).
[13] D. V. Lang, J. Appl. Phys. **45**, 3023 (1974).
[14] R. Langfeld, Appl. Phys. A **44**, 107 (1987).
[15] A. Schary and C. A. Lee, J. Appl. Phys. **67**, 200 (1990).

[16] M. Gal and C. Shwe, Appl. Phys. Lett. **56**, 545 (1990).
[17] J. W. Garland, H. Abad, M. Viccraro, and P. M. Raccah, Appl. Phys. Lett. **52**, 1176 (1988).
[18] D. Fournier and A. C. Boccara, Mater. Sci. Eng. B **5**, 83 (1990).
[19] G. M. Martin, M. L. Verheijke, J. A. J. Jansen, and G. Poiblaud, J. Appl. Phys. **50**, 467 (1979).
[20] M. O. Manasreh, W. C. Mitchel, and D. W. Fischer, Appl. Phys. Lett. **55**, 864 (1989).
[21] By the late S. P. F. Humphreys-Owen, Proc. Phys. Soc. **77**, 949 (1961).
[22] H. J. Lewerenz and N. Dietz, Appl. Phys. Lett. **59**, 1470 (1991).
[23] N. Dietz and H. J. Lewerenz, Appl. Phys. Lett. **60**, 2403 (1992).
[24] H. B. Holl, J. Opt. Soc. Am. **57**, 683 (1967).
[25] P. H. Miller and J. R. Johnson, Physica **XX**, 1026 (1954).
[26] I. N. Bronstein and K. A. Semendjajew, *Taschenbuch der Mathematik*, 19th ed. (Verlag Harri Deutsch, Frankfurt/M., 1980).
[27] J. J. Snyder, Appl. Opt. **19**, 1223 (1980).
[28] M. L. Fearheiley and K. J. Bachmann, *Proceedings of the Symposium on Materials and New Processing Technologies for Photovoltaics*, San Francisco, CA (The Electrochemical Society, Pennington, NJ, 1983), pp. 469–473.
[29] M. L. Fearheiley, N. Dietz, and H. J. Lewerenz, J. Electrochem. Soc. **139**, 512 (1992).
[30] N. Dietz, M. L. Fearheiley, S. Schroetter, and H. J. Lewerenz, Mater. Sci. Eng. B **14**, 101 (1992).
[31] F. R. Kessler, in *Festkörperprobleme*, edited by F. Sauter (Vieweg, Braunschweig, 1963), Vol. II, pp. 1–92.
[32] N. Dietz, thesis, Technical University Berlin, 1991.
[33] J. C. Bourgoin and M. Lannoo, Rev. Phys. Appl. **23**, 863 (1988).
[34] Y. Mochizuki and T. Ikoma, Rev. Phys. Appl. **23**, 747 (1988).
[35] J. Dabrowski and M. Scheffler, Phys. Rev. B **40**, 10 (1989).
[36] D. Stievenard and H. J. v. Bardeleben, Rev. Phys. Appl. **23**, 803 (1988).
[37] S. Miyazawa, K. Watanabe, J. Osaka, and K. Ikuta, Rev. Phys. Appl. **23**, 727 (1988).
[38] A. R. Peaker, in *Landolt-Börnstein: New Series III Vol. 22b Semiconductors*, edited by O. Madelung and M. Schulz (Springer, Berlin, 1987), pp. 596–598.
[39] E. K. Kim, H. Y. Cho, S.-K. Min, S. H. Choh, and S. Namba, J. Appl. Phys. **67**, 1380 (1990).
[40] G. M. Martin, Appl. Phys. Lett. **39**, 747 (1981).
[41] J. I. Nishizawa, Y. Oyama, and K. Dezaki, J. Appl. Phys. **67**, 1884 (1990).
[42] H. G. Grimmeiss, in Ref. 38, p. 678.
[43] P. J. Dean, D. J. Robbins, and S. G. Bishop, J. Phys. C **12**, 5567 (1979).
[44] H. Y. Ueng and H. L. Hwang, J. Phys. Chem. Solids **51**, 11 (1990).
[45] H. Y. Ueng and H. L. Hwang, J. Phys. Chem. Solids **50**, 1297 (1989).
[46] H. J. Lewerenz, K.-D. Husemann, M. Kunst, H. Goslowsky, S. Fiechter, and H. Neff, Mater. Lett. **4**, 198 (1986).
[47] P. Lange, H. Neff, M. L. Fearheiley, and K. J. Bachmann, J. Electron. Mater. **14**, 667 (1985).
[48] J. J. M. Binsma, L. J. Giling, and J. Bloem, J. Lumin. **27**, 35 (1982).
[49] M. Fearheiley, N. Dietz, S. Schroetter, and H. J. Lerwerenz, in *Non-Stoichiometry in Semiconductors*, edited by K. J. Bachmann, H.-L. Hwang, and C. Schwab (Elsivier, North Holland, 1992), pp. 125–131.
[50] H. Y. Ueng and H. L. Hwang, J. Phys. Chem. Solids **51**, 1 (1990).
[51] J. Grzanna (private communication).
[52] W. H. Press, B. P. Flannery, S. A. Teukoslsky, and W. T. Vetterling, in *Numerical Recipes in C* (Cambridge U.P., Cambridge, 1988).